Understanding diffusion-controlled bubble growth in porous media using experiments and simulations

Emre Turkoz, Jeremy Brandman, Deniz Ertas, and Gary L. Hunter
ExxonMobil Technology and Engineering Company, Annandale, New Jersey 08801, USA

(Received 16 August 2022; accepted 6 July 2023; published 28 July 2023)

Nucleation and subsequent expansion of gas bubbles in porous media is relevant to many applications, including oil recovery, carbon storage, and boiling. We have built an experimental setup using microfluidic chips to study the dynamics of bubble growth in porous media. Visualization experiments of the growth of carbon dioxide bubbles in a supersaturated dodecane solution were conducted. We show that bubbles grow as dissolved gas molecules inside the oversaturated liquid diffuse to the gas-liquid interface. Bubbles expanding inside a porous medium displace the liquid phase until the cluster of the gas-filled pores becomes connected to the outlet at the critical gas saturation, which is used as a measure for the total liquid displacement. Our experiments uniquely focus on the growth of a single bubble and show that larger pressure drops lead to faster bubble growth while resulting in lower critical gas saturations. A nonlinear pore-network model is implemented to simulate bubble growth. We compare model predictions for bubble growth dynamics to our experimental results and present the need for further theoretical development to capture deviations from invasion-percolation when a large pressure drop is applied.

DOI: 10.1103/PhysRevE.108.015105

I. INTRODUCTION

Bubbles growing in porous media, as other transport phenomena away from equilibrium, tend to form complex spatial patterns. Familiar examples include diffusion-limited aggregation [1], invasion percolation [2,3], and viscous fingering [4]. While the stability of immiscible displacement between two fluids has been studied extensively in the literature [5–7], pattern formation of a growing bubble inside a supersaturated liquid phase has not been fully understood. This problem gets complicated as nucleation and growth dynamics of the immiscible vapor phase depend on the saturation of the liquid phase along with the characteristics of the porous medium.

Bubble nucleation and growth in porous media are important problems encountered in oil recovery [8], carbon storage [9], enhanced boiling heat transfer [10], and geothermal energy processes [11]. This problem has attracted various experimental and modeling studies directed to understanding the underlying physics. Visualization techniques such as micromodels [12] and x-ray tomography [13,14] have been used, while pore-network models [15,16] and continuum models [17] have been used for modeling purposes. In this study, we focus on the bubble growth in relevance to oil recovery from tight oil reservoirs.

Unconventional resources have significantly changed the landscape of the oil and gas industry. Tight oil reservoirs, accessible through hydraulic fracturing, have accounted for more than 50% of the total oil production in the United States in recent years [18]. In tight oil reservoirs, where initial pressure is above saturation pressure, hydrocarbons are in liquid phase before production [19]. Oil in these pores consists of a mixture of light and heavy molecules. For example, lighter molecules such as methane and ethane, which are in vapor phase at ambient conditions, are dissolved in the liquid phase in the reservoir prior to production. Pure expansion drive occurs while the fluid is above the bubble point pressure and exits the rock matrix as a single-phase liquid. Oil recovery in this stage depends on the composite system compressibility of the rock and liquid. As the pressure drops, the density of the liquid phase drops as well, resulting in expansion and subsequent expulsion of the liquid phase from the pore space. Following pure expansion drive, solution-gas-drive (SGD) is initiated after the pressure drops below the bubble point. SGD is thought to be one of the main recovery mechanisms for tight oil during primary production [20,21]. Below the bubble point, gas molecules such as methane and ethane start to nucleate bubbles inside the pores. A vapor phase forms inside the porous medium displaces the liquid phase gradually. The nucleated gas bubbles grow as pressure is depleted. At this stage, the principal drive mechanism for production is the expulsion of liquid due to expansion of bubbles inside the pores. Figure 1 presents a simplified representation of production from hydraulically fractured tight rocks. The time to fall below bubble point varies from one well to another while the reported times range from only the first few months of operation [20] to more than a year [22]. Considering that most of the wells continue primary production over at least three years [23], we believe understanding and improving SGD can yield significant improvements in oil recovery, which is estimated to be about 10% for primary production from tight oil wells [22].

Bubble nucleation and growth inside porous media during SGD have been studied in the literature before for heavy oil production and CO_2 storage applications, etc. An important parameter identified in these studies is the critical gas saturation, S_{gc}, defined as the volume fraction of the vapor phase where gas flow becomes continuous through a porous medium [24]. After S_{gc} is reached, the gas-oil-ratio of the produced

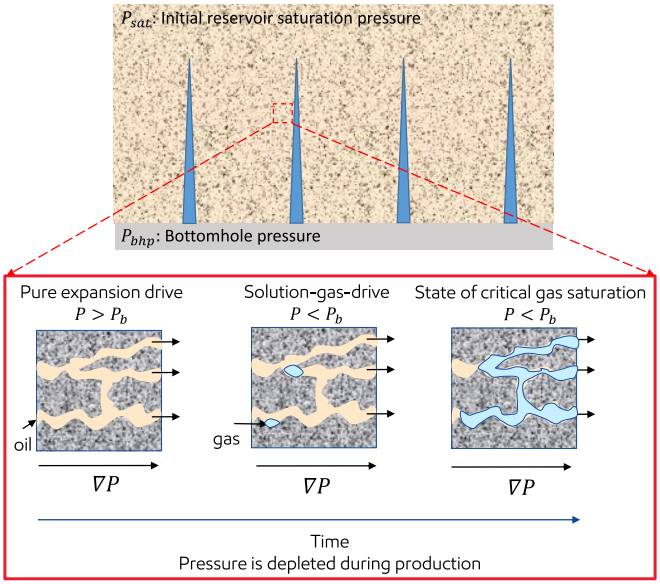

FIG. 1. A simplified representation of production from a tight oil reservoir. Depleting bottom-hole pressure causes hydrocarbons to leave the hydraulically fractured rock. Initial production takes place through pure expansion drive, during which the hydrocarbons are in the liquid phase. After the reservoir pressure drops below the bubble point, solution-gas-drive starts with the nucleation and expansion of gas bubbles. The reservoir eventually reaches the critical gas saturation, S_{gc}, where the gas flow becomes continuous and the liquid production practically stops.

hydrocarbons increase dramatically and the liquid production practically stops. Therefore, doubling S_{gc} typically doubles the recovery from primary production [25]. Reported S_{gc} values for conventional core samples range from 1% to 40% for various experiments [26], and the pressure depletion rate used in experiments is a key factor along with porous media characteristics for the wide spread in the reported values.

Transparent micromodels have been used before in the literature to study SGD [28–35]. Unlike the experiments conducted using cores, transparent microfluidic chips allow for direct visualization of the governing physics such as Ostwald ripening [35], temperature-dependent relative permeability [34], bubble breakup [32], and three-phase flow of gas, oil, and aqueous phases [31,33]. S_{gc} has also been studied using micromodels [28,29] where different pressure decline rates are applied to nucleate and grow bubbles.

The impact of pressure drop with respect to initial saturation pressure, P_{sat}, and pressure decline rate on S_{gc} is crucial to understand, as bottom-hole pressure is likely a controllable parameter during oil production. Some studies performed with microfluidic chips [28,29] have observed S_{gc} to decrease with higher pressure decline rate, i.e., lower pressure decline rates result in larger S_{gc}. This result does not match the outcome of various other studies performed using core scale experiments [26,37], where S_{gc} is measured to be larger for higher pressure decline rates and becomes practically decline rate independent for lower decline rates. In addition to this discrepancy between different studies, two separate explanations [38] have been proposed for the nucleation mechanism behind SGD: (1) instantaneous nucleation [37], where all nucleation sites are activated at once so that S_{gc} becomes pressure decline rate independent; (2) sequential nucleation [39], where the nucleation sites are activated progressively so that higher pressure decline rates result in larger S_{gc}.

A major complication for these previous studies is the combined effect of coupled dynamics of nucleation and bubble growth on S_{gc}. Nucleation is related to the number and the location of the dissolved bubbles while bubble growth is related to how fast the volume of these bubbles expand and the resulting pattern formation. While pressure decline results in increase in bubble volume due to the equation of state, diffusion of dissolved gas molecules inside the solution to the gas-liquid interface also plays a significant role in bubble growth. These two effects take place over two different time scales: Volume increases from pressure drops is governed by hydraulic diffusivity [40], $D_h = k/\mu c\phi$, which depends on the rock porosity, ϕ, permeability, k, fluid compressibility, c, and viscosity, μ, whereas changes from diffusion depend on the diffusivity of gas, D_m, in the solution. D_h is larger than D_m in most cases, and therefore bubble growth due to pressure drop is faster than diffusive growth. These two growth mechanisms should be captured while modeling these systems.

Various pore-network models [15,29] have been developed to simulate bubble growth in porous media. Invasion percolation has been assumed to be the governing mechanism for the bubble growth in these models. Inside a liquid solution with pressure P_l, a gas bubble would start to grow and reach the boundaries of the pores that it spans with pressure P_g. The bubble would keep getting pressurized as gas molecules in the liquid phase diffuse to the gas phase and eventually reaches sufficient pressure to grow into an additional pore. According to invasion percolation, the gas bubble would grow into the neighboring pore with the smallest capillary resistance ($P_g - P_l \geqslant P_c$). The process starts over again and this pore-by-pore invasion scheme continues until the bubble reaches the outlet of the porous medium at S_{gc}.

It has been reported [29] that nucleation is not easily reproducible during experiments since bubbles tend to heterogeneously nucleate around dye particles in solution or dirt stuck on pore walls in microfluidic chips. Our study focuses on the growth dynamics of a single bubble. We study the effect of P_{sat} on bubble growth and critical gas saturation, and eliminate the complication resulting from the nucleation step by initiating bubble growth from a single seed bubble inside the microfluidic chip. Using image processing, we measure the bubble growth rate as a function of P_{sat} and also S_{gc} when the bubble reaches the chip outlet. Using the experimental data, we calculate the capillary number (Ca) observed during bubble growth experiments. We show that high P_{sat} (large pressure declines), or high Ca, lead to deviations from the proposed invasion percolation regime. We also implement a numerical model explained in the literature [29] to model the bubble growth inside a digitized version of our microfluidic chip, and demonstrate the differences between the experiments and the model results to make the case for a more advanced model.

II. EXPERIMENTS

A schematic of the experimental setup and an image of the porous medium inside the microfluidic chip are presented

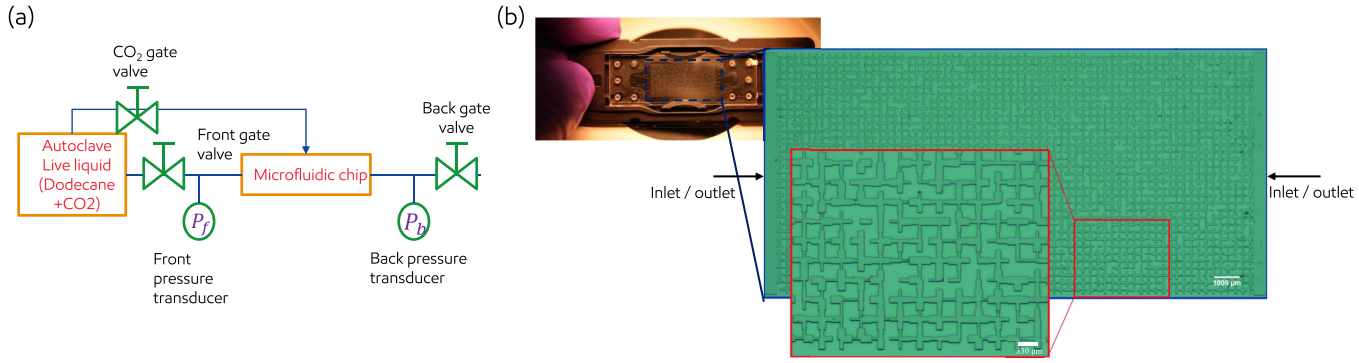

FIG. 2. Experimental setup for microfluidic chip pressurization. (a) Schematic of the flow circuit around the microfluidic chip. Live (gas-saturated) liquid is prepared inside a reactor (autoclave) by pressurizing dodecane with CO_2. Pressure is measured using pressure transducers located upstream and downstream of the chip. The flow path is flushed with CO_2 [27] before the live liquid front gate valve is opened to fill the chip. The imaging system consists of a custom-built microscope with a Nikon 60 mm objective lens and a USB camera. (b) Snapshot of the microfluidic chip consisting of a random network of rectangular channels with 20 μm depth. The channel width varies between 50 and 130 μm. The total volume of the porous medium is 1.6 μl. The porosity is 0.4 while the permeability is 1.6 D. Left and right sides of the chip (marked as inlet/outlet) are accessible while top and bottom sides are blocked.

in Figs. 2(a) and 2(b), respectively. We prepared live (gas-saturated) liquid inside a stainless steel reactor (autoclave) by adding dry ice (CO_2) to liquid dodecane. After the autoclave is sealed, excess CO_2 is purged out of the reactor through a needle valve until the desired initial saturation pressure, P_{sat}, is reached. The autoclave is placed on a magnetic stirrer for at least 24 h before an experiment is conducted to enhance mixing. Microfluidic chips used in this study are commercially available chips through Micronit Microfluidics eV. The chip is made of borosilicate glass, and the geometry consists of a structured network of 7 222 rectangular channels with 20 μm depth. The rectangular channel widths are either 50, 70, 90, 110, or 130 μm, with approximately equal number of channels for each width. As shown in Fig. 2(b), each throat connecting the pores consists of two halves with mostly different widths. Image processing shows that approximately 25% of these half throats are not etched during the manufacturing process, which leads to dead-ends. The lattice length, the distance between the centers of adjacent channels, is about 330 μm, and the total width and length of the porous region are 1 cm and 2 cm, respectively. The total internal volume of the rectangular channels is 1.6 μl. The porosity is 0.4 while the permeability is 1.6 D as supplied by the manufacturer and validated in the laboratory. Before the start of each experiment, the microfluidic chip and the flow circuit around the chip are flushed with CO_2 to get rid of the air in the system. Then, the liquid front gate valve is opened and the microfluidic chip is pressurized with the live (gas-saturated) liquid. Two pressure gauges located in front of the inlet and behind the outlet measure the pressure in the flow circuit. We continued flooding the live liquid until the pressure on both sides of the chip equilibrates and all of the bubbles and CO_2 pockets dissolved in the liquid except for one last bubble, which is used as the seed bubble for bubble growth. We waited until this last bubble becomes smaller than a single pore volume, and depleted the pressure to the atmoshpheric pressure by opening both valves at each end of the microfluidic chip.

Bubble growth starts with the expansion of the pressurized gas bubble as the pressure is depleted to the atmospheric pressure. In our microfluidic chip, the pressure equilibrium, whose time scale depends on D_h as explained above, takes place within the first milliseconds of the depletion. Considering the volume increase at this stage depends on the ratio of the initial pressure with the ambient pressure, we observe that bubbles can grow up to approximately five times for the largest pressure drop we apply in our experiments. This is still not significant as the initial bubble size is smaller than a single channel size. Most of the growth is due to the diffusion of dissolved molecules to the gas phase. A typical bubble shape is shown in Fig. 3(a). The liquid phase is transparent, and the intensity difference between the gas and the liquid phases allows for the detection of the gas phase. Image processing is done using MATLAB software. Bubble volumes are extracted using an image threshold filter followed by segmentation and image dilation. The bubble segmentation is performed with a flood fill by introducing a seed point. Image dilation is performed to fill the holes in the bubble image after the application of the segmentation. We measure the bubble volume, V_b, as a function of time for various P_{sat} values. This data is presented in Fig. 3(b). The bubble volume increases linearly as a function of time. This linear form is expected and has been reported before in the literature for two-dimensional systems [39,41]. The slope of the curves, which corresponds to the bubble growth rate, increases as P_{sat} increases. The experimental data presented in Fig. 3 b also allow for the calculation of the capillary number for these experiments using the formula

$$\text{Ca} = \mu_l u_{\text{bubble}}/\gamma, \tag{1}$$

where $\mu_l = 1.36 \times 10^{-3}$ Pa s [42], u_{bubble} is the effective bubble velocity obtained from the experiments, and $\gamma = 24.7$ mN/m is the surface tension between CO_2 and dodecane [43]. The bubble velocity is calculated by fitting a linear line to the experimental data presented in Fig. 3(b) using the formula $u_{\text{bubble}} = dV_b/A_p dt$, where $A_p = hL_p$ is the characteristic cross-sectional area while $h = 20$ μm is the channel depth and $L_p = 330$ μm is the lattice length. For our experiments, we calculate the limits of Ca as $6.3 \times 10^{-8} < \text{Ca} < 5.2 \times 10^{-5}$.

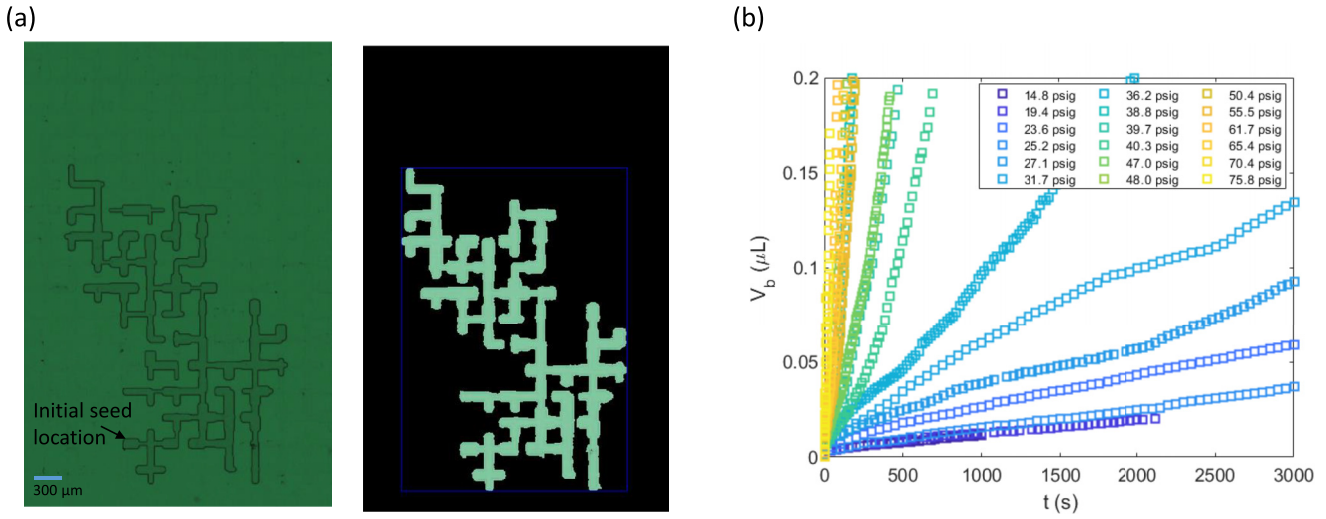

FIG. 3. Bubble growth over time is measured through image processing. (a) Bubble growth pattern for $P_{sat} = 23.6$ psig at $t \approx 1950$ s. The visible phase is the gas phase, while the liquid phase appears transparent. The image obtained using the microscope is post-processed to extract bubble volume at a given time. See the Supplemental Material for the complete video (Video S1 [36]). (b) Bubble volume V_b as a function of time for a subset of our experiments with various supersaturations. The bubble volume growth is approximately linear in time and faster for higher supersaturations. The bubble velocity, u_{bubble}, and the corresponding capillary number, $Ca = \mu_l u_{\text{bubble}}/\gamma$, can be calculated by linear fits to these curves. To calculate the corresponding capillary numbers, we use $\mu_l = 1.36 \times 10^{-3}$ Pa s as the liquid viscosity, and $\gamma = 24.7$ mN/m as the surface tension. The resulting capillary numbers for the complete set of experiments are presented in Fig. 6(d).

The resulting capillary numbers for the complete set of experiments are presented later in Fig. 6(d). A complete bubble growth sequence from the seed to the outlet is presented in Video S2 in the Supplemental Material [36].

In our experiments, one connected bubble continues to invade neighboring pores until it reaches the outlet. When the bubble reaches the outlet, bubble growth takes place in the tubes connecting the chip to the rest of the flow circuit. We measure S_{gc} as the fraction of the pores that is covered by the bubble when the bubble reaches the outlet. Figure 4 a shows how S_{gc} changes as a function of Ca. The two plotting symbols represent two different relative positions of the seed location to the outlet. In our experimental setup, bubbles consistently grow towards the left hand side as shown in Fig. 4(b). We believe this happens because of the small difference in the hydrostatic pressure between the left and the right hand side of the setup, so that it is easier for the bubbles to push the liquid and grow towards left than right. Data points indicated with

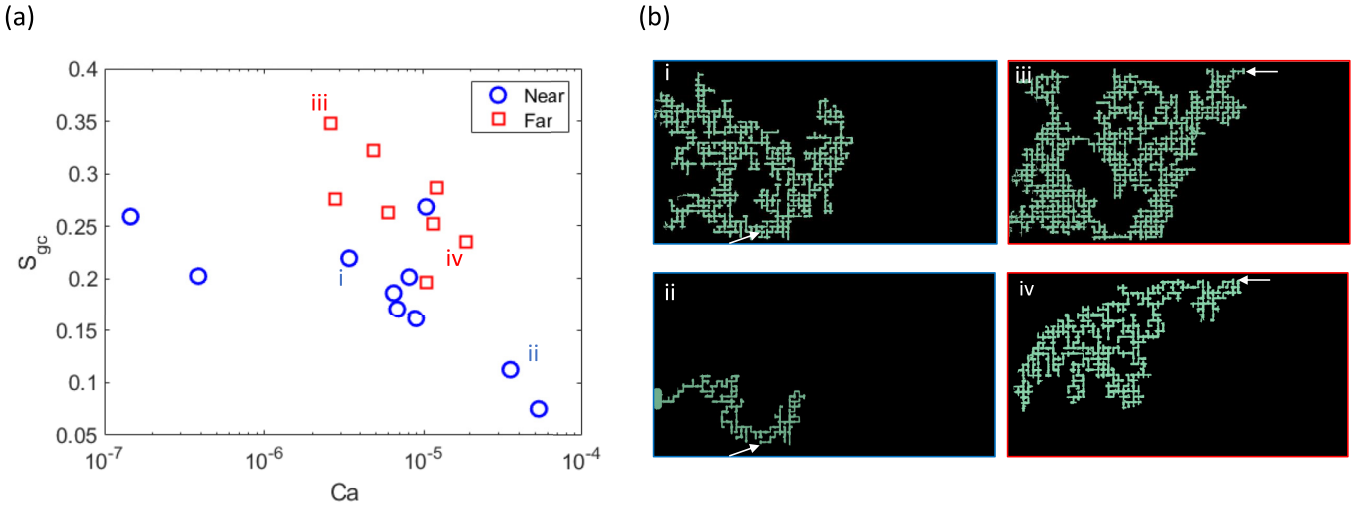

FIG. 4. Critical gas saturation (S_{gc}) is a function of initial bubble location and Ca, which depends on initial saturation P_{sat}. (a) S_{gc} decreases with increasing Ca for both near (s) and far (o) initial bubble locations. The resulting S_{gc} values are larger for the far location because the growing bubble can sweep more liquid until it reaches the outlet. (b) Snapshots of four cases after bubbles reach S_{gc}. Bubbles in higher Ca cases (ii) and (iv) span less volume compared to corresponding lower Ca cases (i) and (iii). Arrows in (i) and (iii) show the locations for the initial bubble for bottom and top cases, respectively. Both sides of the chip connect to a straight channel that extends across the whole width of the chip and acts as outlet.

the *Near* label represent cases where the seed bubble location is closer to the left hand side than those indicated with the *Far* label. The location of the initial seed bubble is indicated by arrows for each case, shown in Figs. 4(b-I) and 4(b-III). Both set of experiments were performed with the same chip layout while one version is the 180° flipped version of the other one. Because the initial seed bubble location is not at the center of the chip, flipping the chip puts the initial seed bubble location to a different distance from the outlet. As Fig. 4(a) shows, S_{gc} strongly depends on the location of the seed bubble, i.e., bubbles starting from the *Far* location result in higher S_{gc} values. This figure also shows that S_{gc} decreases with increasing Ca. As will be discussed shortly, we believe this is due to a deviation from the invasion percolation regime during the bubble growth. For regular drainage processes where a nonwetting fluid displaces a wetting fluid, it has been shown that higher invading fluid velocities (or higher Capillary numbers) lead to less efficient displacement profiles [44]. Here, we show that higher Ca results in less efficient sweep, and growth patterns deviating from invasion percolation are possible during SGD.

III. SIMULATIONS

We have built a pore-by-pore invasion model based on previous work and compared the model and the experiments, which we have shown to deviate from invasion-percolation. The full details of this pore-network model can be found in the literature [28,29]. We will describe the physics captured by the model, and present an overview of the algorithm.

The model handles pore pressurization and pore filling steps separately, as shown in Fig. 5. The transient diffusion equation is solved during the pore pressurization step to calculate the solute flux into the gas phase. The diffusivity of the gas is assumed to be $D_m = 5 \times 10^{-10}$ m^2/s [45]. In this stage, we assume that the bubble volume stays constant, and gas pressure increases due to incoming mass flux. This increase in pressure is calculated using the ideal gas law. When the gas pressure exceeds the sum of the pressure in the liquid and the lowest capillary pressure at the neighboring pores, $P_g \geqslant P_l + P_c$, the pore filling step is initiated. The pore filling step is iterative and starts with an initial guess for the gas pressure after pore filling. During the pore filling step, the bubble expands into the neighboring pore with the lowest capillary pressure. The algorithm also checks if a neighboring pore is part of a dead end with no connection to the outlets and, if so, does not consider these pores for invasion. The Stokes' flow equation is solved to calculate the velocity and the time of filling at the throat connecting the bubble to the neighboring pore to be invaded. The convection-diffusion equation is solved using the Stokes velocity to calculate the influx of molecules during the filling stage. The boundary equation for the convection-diffusion equation is derived from the linear solubility condition [29], $C = P_g/K$, where C is the gas molecule concentration, and K is Henry's constant. To evaluate this concentration value, we calculate the CO_2 molar fraction in the liquid phase as a function of pressure using the commercial PRO/II thermodynamics solver package. Therefore, the estimated pressure also has an effect on the resulting diffusive flux into the gas phase. For the algorithm to converge, the difference between the guessed pressure and the pressure calculated using the ideal gas law with the influx of molecules should be minimized. The guessed pressure is updated using a trust-region algorithm [46]. This process is repeated until the pressure converges and the pore pressurization step is restarted again.

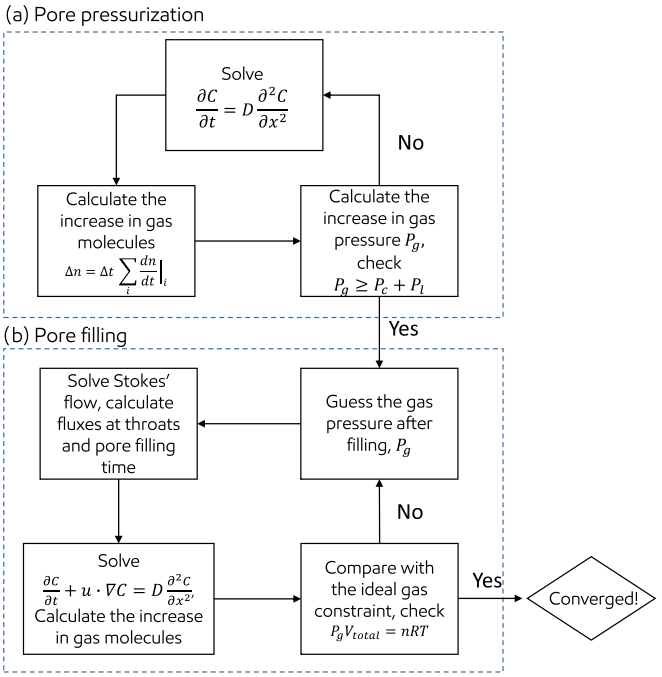

FIG. 5. Numerical algorithm implemented for pore-network simulations. Pore pressurization and pore filling steps are handled separately. The diffusion equation is solved during pore pressurization, and the increase in gas pressure is calculated. This step continues until the gas pressure exceeds the sum of the capillary and the liquid pressure, $P_g \geqslant P_c + P_l$. The pore filling step starts by guessing the gas pressure after the bubble invades the neighboring pore with the lowest capillary pressure. A trust-region algorithm is implemented to guess the pressure correctly. The Stokes' flow equation is solved, velocities at the throats are calculated, and the convection-diffusion equation is solved to calculate the increase in gas molecules in the gas phase, and the increase in pressure. If this increase also satisfies the ideal gas equation, the algorithm has converged at this time step, and the process starts again.

We quantify the compactness of the growth patterns using fractal dimensions, as performed before in the literature for diffusion-limited aggregation [47] and conventional drainage and imbibition experiments [44,48–50]. Figure 6 a shows the total bubble volume normalized by the average single site volume, V_b/V_s, as a function of the growth radius normalized by the lattice length, R_f/l. The growth radius is measured as the diagonal of the smallest square encapsulating the growing bubble at a given time, so that the dimensionless bubble volume would have the functional form

$$V_b/V_s = 0.5(R_f/l)^d, \tag{2}$$

where d is the fractal dimension. We note that for the most efficient displacement the fractal dimension would be $d = 2$. We performed a fit for data obtained for $R_f/l < 30$ in Fig. 6 a, and obtained the fractal dimensions plotted in Fig. 6(b). We picked the condition $R_f/l < 30$ due to practical limits as the

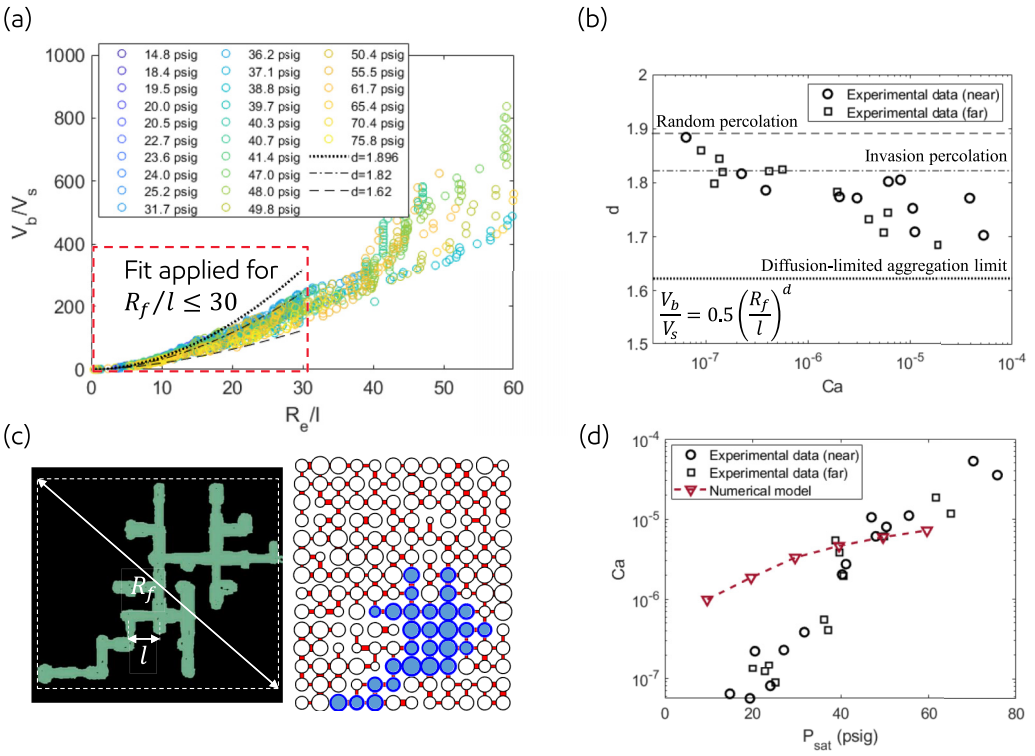

FIG. 6. Fractal dimension analysis quantifies the compactness of the bubble growth pattern and shows deviations from the expected inversion percolation pattern, which is the basis of the numerical model. (a) Dimensionless bubble volume V_b/V_s, where V_s is the average site volume, as a function of dimensionless fractal radius R_f/l, where R_f is evaluated as shown in (c) and $l = 330$ μm is the porous medium lattice length, obtained from experiments. An expanded view of the data in the dashed red box is presented in the Supplemental Material [36]. (b) A power-law fit $[V_b/V_s = 0.5(R_f/l)^d]$ is applied at the early stages ($R_f/l \leqslant 30$) of the data presented in (a) and the fractal dimension d is calculated. d is decreasing as a function of Ca, which implies that bubbles are less compact at larger initial saturations. Uncertainty associated with the determination of the fractal dimension is less than 0.02 within 95% confidence bounds. Fractal dimension limits for random percolation (1.896) [51], invasion percolation with trapping (1.82) [2], and diffusion-limited aggregation (1.62) [52] are shown on the figure with horizontal lines. Simulations also result in a fractal dimension $d = 1.81$ (1.79, 1.83) with 95% confidence bounds. (c) Experimental image showing initial stages of the bubble growth. Fractal radius is calculated by assuming a square pattern growth at early stages. The microfluidic chip is digitized to have an accurate simulation domain for the numerical model. Simulations can capture the pattern of the growth at early stages. (d) Comparison of the numerical model results with the experiments. Experimental bubble growth rates are evaluated using the data presented in Fig. 3(b). Numerical results are evaluated without any fitting parameters.

bubbles at the *Near* location get very close to the outlet. We see that d decreases with Ca, from values near that of invasion percolation towards lower values. Thus, larger saturations result in less compact growth patterns, and therefore less efficient displacement of the liquid inside the porous medium. Figure 6(b) also shows the limits for random percolation [51], invasion percolation with trapping [2], and diffusion-limited aggregation [52].

For our simulations, we digitized our random-network microfluidic chip consisting of rectangular channels connected to pores through rectangular throats. Cylindrical pores are assumed in the simulations, and the volume of each pore is calculated as the sum of the volumes of the channels connected to it using image processing. In practice, the shape of the pores does not play a role in any of the calculation steps. The pore-network model represents the porous medium consisting of pores, for which the pore volume is relevant, and throats, for which the capillary pressure information is relevant. Pores are represented as cylinders as previous examples from the literature, but throats have the correct capillary pressure information which scales with their depth and width for a rectangular cross-section. Therefore, the digitalization process may seem to produce pore-networks that look different than the original domain, but it includes the information required for the model to work properly. As explained above, most of the throats consist of two different widths, and we use the smaller width to define the throat size. Figure 6(c) shows side-by-side an experimental snapshot and a bubble growth pattern obtained through numerical simulations. For these two snapshots, the numerical pattern looks very similar to the experimental one. This similarity breaks down eventually and this deviation takes place at smaller R_f/l for higher Ca. Simulations yield the invasion percolation fractal dimension, 1.81 (1.79, 1.83) with 95% confidence bounds, as expected. Numerical model also gives us the expected bubble growth rate, Ca as a function of P_{sat}. We also calculated the bubble growth rate experimentally by evaluating the slopes of the data presented in Fig. 3(b). The comparison is presented in Fig. 6(d). We note that there are no fitting parameters used for the numerical model to match the experimental data. The experimentally observed values for the bubble growth rate are not exactly obtained by the numerical model, while the

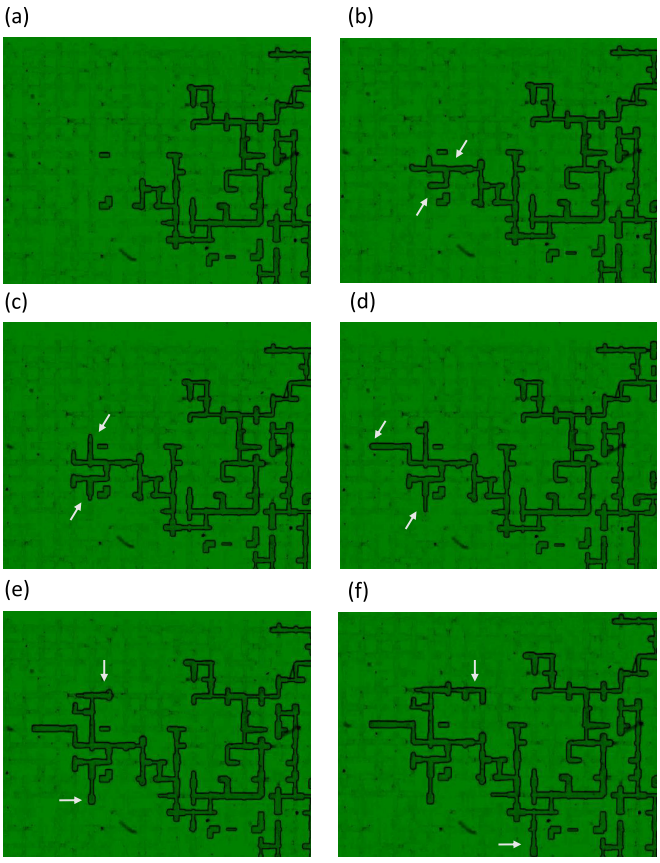

FIG. 7. Snapshots of bubble growth for $P_{sat} = 65.4$ psig at a small section of the porous medium. Frame (a) shows the bubble pattern 172 s after pressure depletion starts. Time between each snapshot is 1 s. Arrows point out the channels that are invaded between each frame. We see multiple pores are invaded at each snapshot.

upward trend of bubble growth rate as a function of P_{sat} is captured.

IV. DISCUSSION

The deviation from invasion percolation, and therefore the mismatch between the experiments and simulations is interesting and deserves further investigation. We performed experiments with a high-speed camera to study if P_{sat} affects the pore-by-pore invasion at early times. Bubble growth for a low pressure case, $P_{sat} = 15$ psig, and for a high pressure case, $P_{sat} = 58$ psig, can be found in Video S3 and Video S4 in the Supplemental Material [36]. These videos show that early stages of bubble growth in both cases follow a pore-by-pore invasion pattern, and deviation from invasion percolation does not seem to take place during very early stages.

However, especially after the bubble reaches a certain size for high P_{sat} values, we observe that multiple pores are invaded at the same time. Figure 7 shows snapshots of bubble growth for $P_{sat} = 65.4$ psig at a small section of the chip. We observe that multiple channels can be invaded at the same time at this stage. We believe the deviation from pore-by-pore invasion takes place at this later stage. This may be happening because the increase in bubble volume also results with a larger surface area, which allows for a high flux of gas molecules into the vapor phase. We also note that our chip consists of channels with five different widths, therefore, the bubble is surrounded with many same-sized channels when it reaches a certain size. The bubble can grow into any of the largest size throats, and the expected invasion percolation path could be different depending on which throat is selected by the bubble. We observe that, at high P_{sat} cases, the bubble is more likely to select the throats in the direction that it already invaded, which results in the decrease of the fractal dimension for higher supersaturations. Pore-network simulations assume that the bubble grows pore-by-pore, CO_2 concentration at every location of the interface is always uniform, and the experimentally observed tendency of the bubble to invade the throats in the direction that it had already invaded is not captured.

V. CONCLUSION

Our study shows the effect of supersaturation on bubble growth dynamics through microfluidics experiments. Starting with seed bubbles at the same location every experiment, we demonstrate that bubble growth is faster with larger initial gas saturation in the liquid phase; however, we sweep less of the volume resulting in a lower liquid recovery. Single bubble growth during SGD has been assumed to be taking place through the invasion percolation mechanism in the literature. We show, to our knowledge for the first time, that the bubble growth pattern can deviate from invasion percolation, and this deviation is enhanced for higher Ca. While bubble growth relies on diffusion and pressure drop to increase volume compared with the conventional drainage, the sweeping efficiency increases with lower Ca, as previously reported in the literature for conventional drainage experiments [44,53]. We also demonstrate that pore-network models developed for bubble growth in porous media have limited applicability to experiments where the deviation from invasion percolation is apparent. More insights can be obtained with a direct numerical simulation approach, where the compressible mass and momentum conservation equations are solved with an equation of state at pore scale.

While insights from this study are relevant for tight oil recovery, it should be kept in mind that porosities, length scales and the resulting permeability values are orders of magnitude different for tight oil systems. In addition to the confinement effects such as bubble point suppression [54,55], liquid slippage [56], and enhanced capillary forces [57], nanometer scale pore sizes also result in smaller advection and diffusion time scales [58,59]. The interplay between governing physics of bubble growth becomes more challenging to understand when the heterogeneous wettability of shale rocks [60–62] and three-phase flow of oil, gas, and water are brought into the picture. Therefore, a systematic study where the insights valid for micrometer-scale porous media are compared with the phenomena observed at nanometer-scale is essential to obtain an overall understanding of SGD relevant to tight oil recovery.

[1] T. A. Witten and L. M. Sander, Diffusion-limited aggregation, Phys. Rev. B **27**, 5686 (1983).

[2] R. Lenormand and C. Zarcone, Invasion Percolation in an Etched Network: Measurement of a Fractal Dimension, Phys. Rev. Lett. **54**, 2226 (1985).

[3] A. Birovljev, G. Wagner, P. Meakin, J. Feder, and T. Jøssang, Migration and fragmentation of invasion percolation clusters in two-dimensional porous media, Phys. Rev. E **51**, 5911 (1995).

[4] J. Stokes, D. Weitz, R. Ball, and A. Kushnick, Viscous fingering instabilities in porous media, in *Time-dependent Effects in Disordered Materials* (Springer, Berlin, 1987), pp. 139–143.

[5] J. P. Stokes, D. A. Weitz, J. P. Gollub, A. Dougherty, M. O. Robbins, P. M. Chaikin, and H. M. Lindsay, Interfacial Stability of Immiscible Displacement in a Porous Medium, Phys. Rev. Lett. **57**, 1718 (1986).

[6] C. Wang, Y. Mehmani, and K. Xu, Capillary equilibrium of bubbles in porous media, Proc. Natl. Acad. Sci. USA **118**, e2024069118 (2021).

[7] C. Zhang, M. Oostrom, T. W. Wietsma, J. W. Grate, and M. G. Warner, Influence of viscous and capillary forces on immiscible fluid displacement: Pore-scale experimental study in a water-wet micromodel demonstrating viscous and capillary fingering, Energy Fuels **25**, 3493 (2011).

[8] E. Hunt Jr and V. Berry Jr, Evolution of gas from liquids flowing through porous media, AIChE J. **2**, 560 (1956).

[9] M. J. Bickle, Geological carbon storage, Nat. Geosci. **2**, 815 (2009).

[10] J. R. Thome, *Enhanced Boiling Heat Transfer*, Tech. Rep. Hemisphere Pub. Corp. (Taylor & Francis, London, 1990).

[11] G. Schubert and J. M. Straus, Two-phase convection in a porous medium, J. Geophys. Res. **82**, 3411 (1977).

[12] L. Zuo, C. Zhang, R. W. Falta, and S. M. Benson, Micromodel investigations of CO_2 exsolution from carbonated water in sedimentary rocks, Adv. Water Resour. **53**, 188 (2013).

[13] L. Zuo, S. Krevor, R. W. Falta, and S. M. Benson, An experimental study of CO_2 exsolution and relative permeability measurements during CO_2 saturated water depressurization, Transp. Porous Media **91**, 459 (2012).

[14] S. Berg, Y. Gao, A. Georgiadis, N. Brussee, A. Coorn, H. van der Linde, J. Dietderich, F. O. Alpak, D. Eriksen, M. Mooijer-van den Heuvel *et al.*, Determination of critical gas saturation by micro-ct, Petrophysics—SPWLA J. Form. Eval. Res. Descr. **61**, 133 (2020).

[15] W. Zhao and M. A. Ioannidis, Gas exsolution and flow during supersaturated water injection in porous media: I. Pore network modeling, Adv. Water Resour. **34**, 2 (2011).

[16] N. Mahabadi, X. Zheng, T. S. Yun, L. van Paassen, and J. Jang, Gas bubble migration and trapping in porous media: Pore-scale simulation, J. Geophys. Res.: Solid Earth **123**, 1060 (2018).

[17] L. Cueto-Felgueroso, X. Fu, and R. Juanes, Pore-scale modeling of phase change in porous media, Phys. Rev. Fluids **3**, 084302 (2018).

[18] S. Balasubramanian, P. Chen, S. Bose, A. Alzahabi, and G. Thakur, Recent advances in enhanced oil recovery technologies for unconventional oil reservoirs, in *Proceedings of the Offshore Technology Conference* (OnePetro, Richardson, TX, 2018).

[19] J. Wan, R. Barnum, D. DiGloria, A. Leahy-Dios, R. Missman, and J. Hemphill, Factors controlling recovery in liquids rich unconventional systems, in *Proceedings of the International Petroleum Technology Conference (IPTC)* (European Association of Geoscientists & Engineers, The Netherlands, 2013), pp. cp–350.

[20] R. S. Jones, Producing gas-oil ratio behavior of tight oil reservoirs, in *SPE/AAPG/SEG Unconventional Resources Technology Conference* (OnePetro, Richardson, TX, 2016).

[21] S. I. Geetan, R. M. MacDonald, and K. Denis, Insights into recovery mechanisms in shales through digital rock technology, in *Proceedings of the SPE/AAPG/SEG Unconventional Resources Technology Conference* (OnePetro, Richardson, TX, 2016).

[22] B. Kong, S. Wang, and S. Chen, Simulation and optimization of CO2 huff-and-puff processes in tight oil reservoirs, in *Proceedings of the SPE Improved Oil Recovery Conference* (OnePetro, Richardson, TX, 2016).

[23] H. Wachtmeister, L. Lund, K. Aleklett, and M. Höök, Production decline curves of tight oil wells in eagle ford shale, Nat. Resour. Res. **26**, 365 (2017).

[24] A. Firoozabadl, B. Ottesen, and M. Mikkelsen, Measurements of supersaturation and critical gas saturation, SPE Form. Eval. **7**, 337 (1992).

[25] J. Kamath and R. Boyer, Critical gas saturation and supersaturation in low-permeability rocks, SPE Form. Eval. **10**, 247 (1995).

[26] A. Firoozabadi, Mechanisms of solution gas drive in heavy oil reservoirs, J. Can. Pet. Technol. **40**, 15 (2001).

[27] A. T. Krummel, S. S. Datta, S. Münster, and D. A. Weitz, Visualizing multiphase flow and trapped fluid configurations in a model three-dimensional porous medium, AIChE J. **59**, 1022 (2013).

[28] X. Li and Y. Yortsos, Visualization and numerical studies of bubble growth during pressure depletion, in *Proceedings of the SPE Annual Technical Conference and Exhibition* (OnePetro, Richardson, TX, 1991).

[29] X. Li and Y. Yortsos, Visualization and simulation of bubble growth in pore networks, AIChE J. **41**, 214 (1995).

[30] A. Chatenever, M. K. Indra, and J. R. Kyte, Microscopic observations of solution gas-drive behavior, J. Pet. Technol. **11**, 13 (1959).

[31] D. George, O. Hayat, and A. Kovscek, A microvisual study of solution-gas-drive mechanisms in viscous oils, J. Pet. Sci. Eng. **46**, 101 (2005).

[32] R. Bora, B. Maini, and A. Chakma, Flow visualization studies of solution gas drive process in heavy oil reservoirs using a glass micromodel, SPE Reser. Eval. Eng. **3**, 224 (2000).

[33] F. Huang, R. Xu, P. Jiang, C. Wang, H. Wang, and Z. Lun, Pore-scale investigation of CO_2/oil exsolution in CO_2 huff-n-puff for enhanced oil recovery, Phys. Fluids **32**, 092011 (2020).

[34] T. Lu, Z. Li, S. Li, S. Liu, X. Li, P. Wang, and Z. Wang, Behaviors of foamy oil flow in solution gas drive at different temperatures, Transp. Porous Media **109**, 25 (2015).

[35] R. Xu, R. Li, F. Huang, and P. Jiang, Pore-scale visualization on a depressurization-induced CO_2 exsolution, Sci. Bull. **62**, 795 (2017).

[36] See Supplemental Material at http://link.aps.org/supplemental/10.1103/PhysRevE.108.015105 for videos S1–S4.

[37] A. Firoozabadi and D. Kashchiev, Pressure and volume evolution during gas phase formation in solution gas drive process (includes associated papers 38340 and 38565), Spe J. **1**, 219 (1996).

[38] C. Du and Y. Yortsos, A numerical study of the critical gas saturation in a porous medium, Transp. Porous Media **35**, 205 (1999).

[39] X. Li and Y. Yortsos, Theory of multiple bubble growth in porous media by solute diffusion, Chem. Eng. Sci. **50**, 1247 (1995).

[40] M. A. Grant and M. L. Sorey, The compressibility and hydraulic diffusivity of a water-steam flow, Water Resour. Res. **15**, 684 (1979).

[41] A. Dominguez, S. Bories, and M. Prat, Gas cluster growth by solute diffusion in porous media. experiments and automaton simulation on pore network, Int. J. Multiphase Flow **26**, 1951 (2000).

[42] D. Caudwell, J. Trusler, V. Vesovic, and W. Wakeham, The viscosity and density of n-dodecane and n-octadecane at pressures up to 200 MPa and temperatures up to 473 K, Int. J. Thermophys. **25**, 1339 (2004).

[43] A. Georgiadis, F. Llovell, A. Bismarck, F. J. Blas, A. Galindo, G. C. Maitland, J. M. Trusler, and G. Jackson, Interfacial tension measurements and modelling of (carbon dioxide+n-alkane) and (carbon dioxide+water) binary mixtures at elevated pressures and temperatures, J. Supercrit. Fluids **55**, 743 (2010).

[44] B. Zhao, C. W. MacMinn, and R. Juanes, Wettability control on multiphase flow in patterned microfluidics, Proc. Natl. Acad. Sci. USA **113**, 10251 (2016).

[45] S. P. Cadogan, B. Mistry, Y. Wong, G. C. Maitland, and J. M. Trusler, Diffusion coefficients of carbon dioxide in eight hydrocarbon liquids at temperatures between (298.15 and 423.15) K at pressures up to 69 MPa, J. Chem. Eng. Data **61**, 3922 (2016).

[46] C. T. Kelley, *Iterative Methods for Linear and Nonlinear Equations* (SIAM, Philadelphia, PA, 1995).

[47] J. M. Tenti, S. N. Hernandez Guiance, and I. M. Irurzun, Fractal dimension of diffusion-limited aggregation clusters grown on spherical surfaces, Phys. Rev. E **103**, 012138 (2021).

[48] K. J. Maloy, L. Furuberg, J. Feder, and T. Jossang, Dynamics of Slow Drainage in Porous Media, Phys. Rev. Lett. **68**, 2161 (1992).

[49] M. Nadafpour and M. R. Rasaei, Investigating drainage rate effects on fractal patterns and capillary fingering in a realistic glass micromodel, Tehnicki vjesnik/Technical Gazette **21**, 1263 (2014).

[50] O. I. Frette, K. J. Maløy, J. Schmittbuhl, and A. Hansen, Immiscible displacement of viscosity-matched fluids in two-dimensional porous media, Phys. Rev. E **55**, 2969 (1997).

[51] M. A. Knackstedt, M. Sahimi, and A. P. Sheppard, Nonuniversality of invasion percolation in two-dimensional systems, Phys. Rev. E **65**, 035101(R) (2002).

[52] K. J. Måløy, J. Feder, and T. Jøssang, Viscous Fingering Fractals in Porous Media, Phys. Rev. Lett. **55**, 2688 (1985).

[53] R. Lenormand, E. Touboul, and C. Zarcone, Numerical models and experiments on immiscible displacements in porous media, J. Fluid Mech. **189**, 165 (1988).

[54] J. Zhong, Y. Zhao, C. Lu, Y. Xu, Z. Jin, F. Mostowfi, and D. Sinton, Nanoscale phase measurement for the shale challenge: Multicomponent fluids in multiscale volumes, Langmuir **34**, 9927 (2018).

[55] Y. Zhao, Y. Wang, J. Zhong, Y. Xu, D. Sinton, and Z. Jin, Bubble point pressures of hydrocarbon mixtures in multiscale volumes from density functional theory, Langmuir **34**, 14058 (2018).

[56] D. Fan, W. Wang, A. Ettehadtavakkol, and Y. Su, Confinement facilitates wetting liquid slippage through mixed-wet and heterogeneous nanoporous shale rocks, in *Proceedings of the SPE/AAPG/SEG Unconventional Resources Technology Conference* (OnePetro, Richardson, TX, 2019).

[57] M. Alfi, B. Yan, Y. Cao, C. An, Y. Wang, J. He, and J. Killough, How to improve our understanding of gas and oil production mechanisms in liquid-rich shale, in *Proceedings of the SPE Annual Technical Conference and Exhibition* (OnePetro, Richardson, TX, 2014).

[58] M. Fleury and M. Romero-Sarmiento, Characterization of shales using T_1-T_2 NMR maps, J. Pet. Sci. Eng. **137**, 55 (2016).

[59] B. Ling, A. M. Tartakovsky, and I. Battiato, Dispersion controlled by permeable surfaces: Surface properties and scaling, J. Fluid Mech. **801**, 13 (2016).

[60] H. J. Deglint, C. DeBuhr, C. R. Clarkson, F. F. Krause, S. Aquino, A. Vahedian, and A. Ghanizadeh, Understanding wettability heterogeneity at the micro- and nanoscale in unconventional light oil reservoirs, in *Proceedings of the Unconventional Resources Technology Conference* (Society of Exploration Geophysicists, American Association of Petroleum Geologists, Tulsa, OK, 2016), pp. 2777–2789.

[61] H. Deglint, A. Ghanizadeh, C. DeBuhr, C. Clarkson, and J. W. Wood, Comparison of micro-and macro-wettability measurements for unconventional reservoirs: The devil is in the detail, in *Proceedings of the SPE/AAPG/SEG Unconventional Resources Technology Conference* (OnePetro, Richardson, TX, 2017).

[62] M. G. Kibria, Q. Hu, H. Liu, Y. Zhang, and J. Kang, Pore structure, wettability, and spontaneous imbibition of Woodford Shale, Permian Basin, West Texas, Mar. Pet. Geol. **91**, 735 (2018).